AIAA JOURNAL
Vol. 30, No. 8, August 1992

Simplified Linear Stability Transition Prediction Method for Separated Boundary Layers

Paolo Dini*
Carleton College, Northfield, Minnesota 55057
and
Michael S. Selig† and Mark D. Maughmer‡
Pennsylvania State University, University Park, Pennsylvania 16802

An existing transition prediction method for attached, two-dimensional, incompressible boundary layers based on linear stability analysis is extended to separated, two-dimensional, incompressible boundary layers such as those found in laminar (transitional) separation bubbles. It is shown why the present method, which tracks the growth of disturbances at many different frequencies, is more accurate than the so-called envelope methods for nonsimilar boundary-layer developments. Reliance on a database of precalculated stability characteristics of known velocity profiles makes this method much faster than traditional stability calculations of similar accuracy. The Falkner-Skan self-similar profiles are used for attached flow, and a new, very general family of profiles is used for separated flow. Comparisons with measured transition locations inside the bubble show good agreement over the range of chord Reynolds numbers and airfoil angles of attack of interest.

Nomenclature

b = width of separated shear layer
C_p = pressure coefficient, $p - p_\infty/\frac{1}{2}\rho U_\infty^2$
c = airfoil chord
c_f = skin-friction coefficient
f = disturbance frequency, Hz
G = amplitude of Coles's wake function
H_{12} = boundary-layer shape factor, δ_1/δ_2
H_{32} = boundary-layer shape factor, δ_3/δ_2
h = distance of bottom of shear layer from airfoil surface
N = amplification factor at constant frequency
$\overline{N}$ = unscaled amplification factor at constant frequency
n = linear stability theory amplification factor
n_{crit} = value of n at transition
p = static pressure along the airfoil surface
R = chord Reynolds number, $U_\infty c/\nu$
R_{δ_2} = momentum thickness Reynolds number, $U\delta_2/\nu$
s = streamwise coordinate from the stagnation point
U = boundary-layer edge velocity
u = streamwise velocity inside the boundary layer
x = distance along airfoil chord from leading edge
y = normal distance from the surface
α^* = complex wave number of sinusoidal disturbance
α_i = dimensionless amplification rate, $\mathrm{Im}(\alpha^*\delta_2)$
β = Falkner-Skan pressure gradient parameter, $\xi^2/\nu\,(dU/ds)$
δ = boundary-layer thickness
δ_1 = boundary-layer displacement thickness
δ_2 = boundary-layer momentum thickness
δ_3 = boundary-layer kinetic energy thickness
η = Falkner-Skan similarity variable, y/ξ
μ = molecular viscosity of air
ν = kinematic viscosity of air, μ/ρ
ξ = Falkner-Skan characteristic thickness
ρ = density of air
ω^* = radian frequency of sinusoidal disturbance
ω = dimensionless radian frequency, $\omega^*\delta_2/U$

Received Aug. 5, 1991; presented as Paper 91-3285 at the AIAA 9th Applied Aerodynamics Conference, Baltimore, MD, Sept. 22–26, 1991; revision received Feb. 4, 1992; accepted for publication Feb. 5, 1992.

*Research Associate, Department of Mathematics and Computer Science. Member AIAA.
†Research Assistant, Department of Aerospace Engineering. Student Member AIAA.
‡Associate Professor, Department of Aerospace Engineering. Senior Member AIAA.

Introduction

THE prediction of boundary-layer transition has been the object of research in fluid mechanics and aerodynamics for over half a century. The methods used today can be divided into two classes: empirical correlations and semiempirical methods. One of the most widely used correlations is due to Michel,[1] who related the transition Reynolds number based on the distance from the stagnation point on an airfoil to the value of the momentum thickness Reynolds number at transition. A similar criterion was developed by Eppler,[2] who related the momentum thickness Reynolds number to the energy to the momentum thickness shape factor at transition. A different approach was developed by van Ingen[3] and independently by Smith and Gamberoni.[4] A linear stability analysis of the governing equations is performed, and transition is assumed to take place when the amplification factor reaches a value previously correlated to experimentally observed transition locations. The amplification factor, denoted $n(s)$, is defined as the natural logarithm of the ratio of disturbance amplitude at station s to its amplitude at neutral stability, s_0. For similar flow environments the transition, or critical, value of the amplification factor has been reported to be about 9 by many researchers. In this approach, rather than correlating characteristic parameters of the flow arbitrarily, an attempt is made to model the actual physical process by which transition occurs. Linear stability theory, in fact, directly models the growth of instabilities in a boundary layer while indirectly, through the boundary-layer development, accounting for the effects of Reynolds number. Because of the empirical input regarding the value of n at transition, the e^n method is referred to as semiempirical.

The major advantage of the e^n method is its ability to account for the effect of the upstream boundary-layer development on the stability of the boundary layer. In contrast, empirical correlations such as Michel's and Eppler's simply monitor local boundary-layer parameters and indicate transition when a certain local condition has been met, irrespective of the upstream history. The main disadvantage of the exact formulation of the e^n method, however, is that it requires very long calculation times. The most widely used such method is the SALLY program[5] which, in fact, requires hours of CPU time on a mainframe for a single-angle-of-attack airfoil analysis.

To make linear stability theory easily accessible for routine applications, a number of approximations have been developed. In the present paper three will be discussed: 1) the envelope methods of Gleyzes et al.,[6] 2) the envelope methods of Drela and Giles,[7] and 3) the approximate method of Stock and Degenhart.[8] Since the envelope methods are faster than Stock and Degenhart's method, they would be the preferred choice for use in the airfoil design process. The need to make an informed decision as to which of these two approaches to follow has motivated the careful analysis of their differences and similarities that is presented in this paper. It is shown that envelope methods lead to errors for nonsimilar boundary-layer developments and, therefore, that the method of Stock and Degenhart is preferable in spite of its longer calculation time. More importantly, Stock and Degenhart's method is not limited to the Falkner-Skan profiles as the envelope methods but can be applied to any arbitrarily defined family of profiles.

The method of Ref. 8 was developed for incompressible boundary layers developing between stagnation and laminar separation. In the present work this method is extended to separated boundary layers. Typical aerodynamic boundary-layer flows that do not reach transition before laminar separation do so as a free shear layer and usually reattach as a turbulent boundary layer, thereby forming a laminar (or transitional) separation bubble. In the course of developing a model for such bubbles, as reported in Ref. 9, the need for an accurate transition model led to the present study.

Theoretical Background

Rather than performing a linear stability analysis of the boundary-layer velocity profile as can be obtained, for instance, from a finite difference method at each downstream station, approximate methods make use a database of the stability characteristics of the Falkner-Skan profiles that is computed in advance. This database is then accessed during a boundary-layer calculation using the local shape factor and Reynolds number as coupling parameters. More precisely, the nondimensional growth rate $-\alpha_i$, corresponding to a particular value of the local shape factor of a Falkner-Skan profile and of the local Reynolds number, is divided by the local boundary-layer characteristic thickness (i.e., the momentum thickness δ_2) to obtain the physical growth rate.

Given that the correct characteristic thickness is obtained independently, from the momentum integral equation, the manner in which the nondimensional database is generated is of no consequence. The most convenient way is to calculate the growth rates for self-similar developments at constant H_{12} values and increasing R_{δ_2}. Starting from the Orr-Sommerfeld spatial instability analysis of the Falkner-Skan profiles at many different values of H_{12}, a set of neutral curves (for which $\alpha_i = 0$) is generated, one for each value of shape factor. An example of these neutral curves is shown in Fig. 1 for two values of H_{12}. For each value of shape factor, the nondimensional amplification rate, $-\alpha_i$, is evaluated along rays of constant reduced frequency,

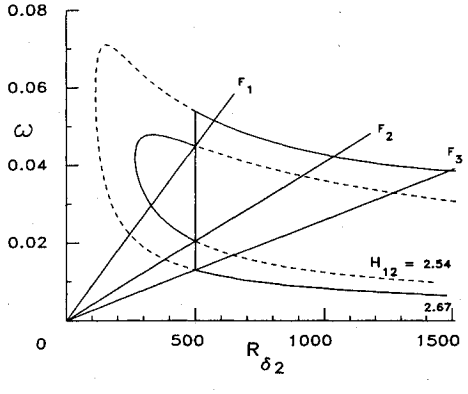

Fig. 1 Neutral curves for two values of H_{12}.

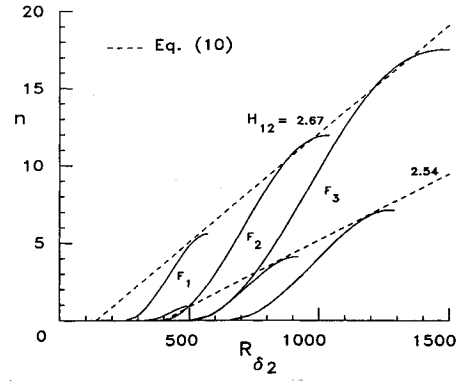

Fig. 2 Amplification curves for two values of H_{12}.

$$F = \frac{2\pi f \nu}{U^2} = \frac{2\pi f(\delta_2/U)}{(U\delta_2/\nu)} = \frac{\omega}{R_{\delta_2}} \tag{1}$$

to form curves $-\alpha_i(R_{\delta_2}, H_{12}, F)$. The amplification factor for the development of each Falkner-Skan profile can be found from these curves. The definition of the amplification factor for a fixed-frequency disturbance is

$$N(R_{\delta_2}, H_{12}, F) = \int_{s_0}^{s} -\alpha_i^* \, ds = \int_{R_{\delta_{2_0}}}^{R_{\delta_2}} \frac{-\alpha_i^*}{(dR_{\delta_2}/ds)} \, dR_{\delta_2} \tag{2}$$

where the asterisk denotes a physical variable. For a Falkner-Skan profile,

$$R_{\delta_2} = \frac{U\delta_2}{\nu} = \frac{U}{\nu}\left[\left(\frac{2}{1+m}\frac{\nu s}{U}\right)^{1/2}\int_0^\infty f'(1-f')\,d\eta\right] \tag{3}$$

where f is the dimensionless Falkner-Skan streamfunction, and m is constant and defined as

$$m(H_{12}) = \frac{s}{U}\frac{dU}{ds} \tag{4}$$

Denoting the momentum thickness integral (not a function of s) by I,

$$I(H_{12}) = \int_0^\infty f'(1-f')\,d\eta \tag{5}$$

the spatial derivative of the momentum thickness Reynolds number becomes

$$\frac{dR_{\delta_2}}{ds} = \frac{I^2}{\delta_2} \tag{6}$$

Thus, Eq. (2) can be written as

$$N(R_{\delta_2}, H_{12}, F) = \frac{1}{I^2}\int_{R_{\delta_{2_0}}}^{R_{\delta_2}} -(\alpha_i^*\delta_2)\,dR_{\delta_2} = \frac{1}{[I(H_{12})]^2}\int_{R_{\delta_{2_0}}}^{R_{\delta_2}} -\alpha_i(R_{\delta_2}, H_{12}, F)\,dR_{\delta_2} \tag{7}$$

In this way the original dimensionless eigenvalues of the dimensionless Orr-Sommerfeld equation can be used to find N, which is defined in terms of a dimensional wave number and distance. This can be done for a self-similar profile, since dR_{δ_2}/ds assumes the particular form shown. The curves ob-

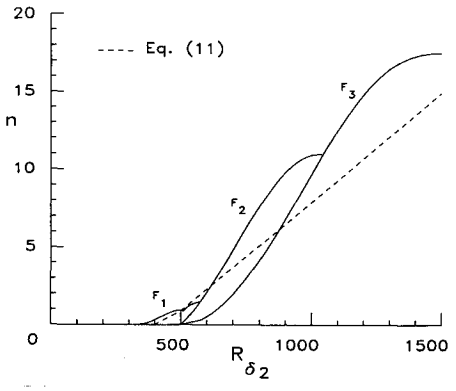

Fig. 3 Growth of n through the step in H_{12}.

tained with this integral for different frequencies and at constant H_{12} are shown in Fig. 2.

An alternative way to construct the database, the method followed by Stock and Degenhart,[8] is to store the result of the integration of the dimensionless wave number over the same Reynolds number ranges and for the same reduced frequencies:

$$\overline{N}(R_{\delta_2}, H_{12}, F) = \int_{R_{\delta_{1_0}}}^{R_{\delta_1}} -\alpha_i(R_{\delta_1}, H_{12}, F)\, dR_{\delta_1} \tag{8}$$

where δ_1 is the preferred characteristic thickness. During a boundary-layer calculation, at each downstream station the (varying) reduced frequency is extracted from the desired constant physical frequency using Eq. (1), and is then used together with the local values of shape factor and Reynolds number to access the correct value of $\overline{N}$. Using its neighboring values, the derivative $d\overline{N}/dR_{\delta_1} = -\alpha_i$ can be evaluated and then used in

$$N(s, f) = \int_{s_0}^{s} \frac{-\alpha_i}{\delta_1}\, ds \tag{9}$$

In this integral δ_1 is given by the boundary-layer development. The envelope of a series of such N growths is the desired $n(s)$ development.

Approximate Envelope Methods

In Refs. 6 and 7 the envelope of the integrals given by Eq. (7) for each value of H_{12} is approximated as a straight line. This leads to the following expression for the amplification surface for self-similar developments:

$$n(R_{\delta_2}, H_{12}) = \left[\frac{dn}{dR_{\delta_2}}(H_{12})\right]^e [R_{\delta_2} - R_{\delta_{2_0}}(H_{12})] \tag{10}$$

where the superscript e denotes a value obtained from the straight-line envelope of amplified frequencies, the actual functions for which are given in Ref. 7. Whereas in Ref. 6 the amplification integral is evaluated as

$$n(s) = \int_{R_{\delta_{2_0}}}^{R_{\delta_2}(s)} \left[\frac{dn}{dR_{\delta_2}}(H_{12})\right]^e dR_{\delta_2} \tag{11}$$

in Ref. 7 the variable of integration is changed back to s:

$$n(s) = \int_{s_0}^{s} \left[\frac{dn}{dR_{\delta_2}}(H_{12})\right]^e \frac{dR_{\delta_2}}{ds}\, ds \tag{12}$$

It is shown in Ref. 9 that the expression for dR_{δ_2}/ds used in Ref. 7 equals Eq. (6):

$$\frac{dR_{\delta_2}}{ds} = \frac{1}{\delta_2}\frac{m(H_{12}) + 1}{2} l(H_{12}) = \frac{[I(H_{12})]^2}{\delta_2} \tag{13}$$

where

$$l(H_{12}) = \frac{U\delta_2^2}{\nu s} \tag{14}$$

Using Eqs. (2) and (6), the integrand in Eq. (11) can be written as

$$\left[\frac{dn}{dR_{\delta_2}}(H_{12})\right]^e = \frac{[-\alpha_i^*]^e}{(I^2/\delta_2)} \tag{15}$$

Here $[-\alpha_i^*]^e$ is that distribution of α_i on or near each amplification rate surface $\alpha_i(R_{\delta_2}, \omega)$ for each value of H_{12} that corresponds to the straight-line envelope of the n growths. Using Eqs. (13) and (15), then, the integral for evaluating $n(s)$ used in Ref. 7:

$$n(s) = \int_{s_0}^{s} \left[\frac{dn}{dR_{\delta_2}}(H_{12})\right]^e \frac{m(H_{12}) + 1}{2}\frac{l(H_{12})}{\delta_2(s)}\, ds \tag{16}$$

can be written,

$$n(s) = \int_{s_0}^{s} \frac{[-\alpha_i^*]^e}{(I^2/\delta_2)}\frac{I^2}{\delta_2(s)}\, ds \tag{17}$$

where $\delta_2(s)$ is taken from the nonsimilar boundary-layer development as calculated by the momentum and energy integral equations. Canceling the I:

$$n(s) = \int_{s_0}^{s} \frac{[-\alpha_i^*\delta_2]^e}{\delta_2(s)}\, ds = \int_{s_0}^{s} \frac{[-\alpha_i]^e}{\delta_2(s)}\, ds \tag{18}$$

This expression is identical to that used by Stock and Degenhart[8] except that α_i belongs to the "envelope locus" rather than to the constant reduced-frequency rays. Using $\delta_1(s)$, $R_{\delta_2}(s)$, or $\delta_2(s)$ as calculated by the governing equations is precisely what enables all these methods to account for upstream history on the growth of n. That is, the dimensionless growth rate $-\alpha_i$, obtained at each downstream station from the values of H_{12} and R_{δ_2}, is divided by the local boundary-layer momentum thickness, which is in general different from the value in a self-similar development at the same values of H_{12} and R_{δ_2}.

Error for Nonsimilar Developments

It would seem at first that all three methods of calculating n are equivalent; that is, Eqs. (9) and (18) would appear to lead to the same $n(s)$. The envelope methods developed in both Refs. 6 and 7, however, introduce an error in the evaluation of n that increases in magnitude depending on how much the boundary-layer development diverges from self-similarity. Since all three methods utilize the characteristic thickness from the nonsimilar boundary-layer development correctly, the difference between the envelope methods and Stock and Degenhart's method must lie in the dimensionless value of α_i accessed.

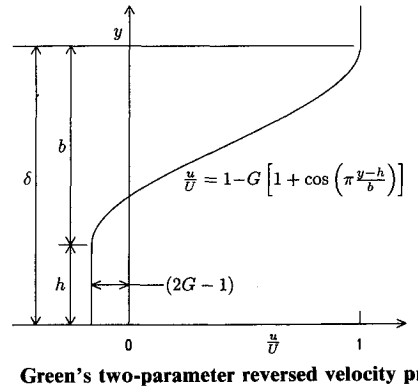

Fig. 4 Green's two-parameter reversed velocity profile.

Even if the actual envelope of the amplification curves were used instead of the straight-line approximation, the $n(s)$ development would not correspond to the true envelope of the amplification curves at constant frequency along the airfoil surface. It is important to emphasize, however, that this error does not arise from taking the envelope in advance rather than at run time. In fact, although it is true that the operations of taking the envelope of a family of functions and integrating each function over a set interval generally do not commute, such a statement does not apply to either of the methods used in Refs. 6 or 7. In these envelope methods, in fact, the envelope is taken *after* the integration is performed in Reynolds number space and is therefore entirely permissible.

To understand why the envelope of Eq. (9) with respect to frequency (after duly exchanging δ_2 for δ_1) does not equal Eq. (18) for nonsimilar developments, it is necessary to examine Eq. (11) more closely. Equation (11) gives the amplification factor as the integral of the derivative of Eq. (10) with respect to R_{δ_2}. In Ref. 6 this equation is proposed and used with the assumption that integrating the local growth rate of a self-similar profile at the local value of the shape factor with respect to Reynolds number is sufficiently accurate for obtaining the amplification factor in a nonsimilar development. However, since the amplification factor is affected by variations in both R_{δ_2} and H_{12}, it is more correct to retain the total differential of the amplification factor surface. In general, using generic Reynolds number and shape factor symbols,

$$n(s) = \int_{R_0}^{R} \frac{\partial n}{\partial R}\,\mathrm{d}R + \int_{H_0}^{H} \frac{\partial n}{\partial H}\,\mathrm{d}H$$

$$= \int_{R_0}^{R} \left(\frac{\partial n}{\partial R} + \frac{\partial n}{\partial H}\frac{\mathrm{d}H}{\mathrm{d}R}\right)\mathrm{d}R$$

$$= \int_{s_0}^{s} \left(\frac{\partial n}{\partial R} + \frac{\partial n}{\partial H}\frac{\mathrm{d}H}{\mathrm{d}R}\right)\frac{\mathrm{d}R}{\mathrm{d}s}\,\mathrm{d}s \qquad (19)$$

In Eq. (19), $\mathrm{d}H/\mathrm{d}R$ and $\mathrm{d}R/\mathrm{d}s$ are obtained from the boundary-layer development to ensure path dependency, as above, and the partial derivatives can be obtained from the self-similar profiles. However, the problem with this formulation is that Eq. (10) cannot be used directly to obtain the partial derivative $\partial n/\partial H$ because $\partial n/\partial H$ is a function of $\mathrm{d}H/\mathrm{d}R$ in addition to H and R. More precisely, Eq. (10) gives the correct value of $\partial n/\partial H$ for the limiting case $\mathrm{d}H/\mathrm{d}R = 0$, which is of no practical utility.

The preceding argument shows that, to make an envelope method and Stock and Degenhart's method entirely equivalent, it would be necessary to construct a database utilizing the self-similar profiles from which the function $\partial n/\partial H(R, H, \mathrm{d}H/\mathrm{d}R)$ could be splined. This effort seems at least equivalent to that required to develop Stock and Degenhart's[8] method itself. Since the construction of the database for an envelope method relies on the explicit knowledge of $\mathrm{d}R/\mathrm{d}s$, however, it would still not be extendable to arbitrary families of profiles such as the one that will be discussed later for separated boundary layers.

To demonstrate the differences between the methods of Refs. 7 and 8, it is helpful to envision a boundary-layer development made up of two constant-H_{12} lengths with a discontinuous jump in between. Figure 1 shows the neutral curves corresponding to the two values of shape factor. It is desired to compare the growth of n obtained by following the development through the jump in H_{12} at constant frequency to that obtained using Eq. (11). Figure 2 shows the amplification curves for the three reduced frequencies shown on the neutral curves plot as calculated by Eq. (7) together with the envelopes given by Eq. (10) for the two values of H_{12}. Figure 3 shows the n-growth along the boundary layer with the switch in shape factor occurring at $R_{\delta_2} = 500$.

The three frequencies selected represent limiting cases that serve best to elucidate the argument. As seen in Fig. 3, as R_{δ_2} increases, $N(F_1)$ grows according to Fig. 2 up to the maximum and, just as it is ready to start decaying, the jump in H_{12} forces further amplification until the upper branch of the neutral curve corresponding to $H_{12} = 2.67$ is crossed. This additional growth will not necessarily be steeper than the envelope. $N(F_2)$ does not start to become amplified until the switch occurs, at which point it grows quite steeply in accordance with the greater area under the amplification rate surface $-\alpha_i(R_{\delta_2}, 2.67, \omega)$. This curve does not necessarily exceed the envelope. Starting with the F_3 curve, at all lower frequencies the growths of N will follow the $H_{12} = 2.67$ envelope, which is parallel to but greater than that given by Eq. (11).

In this example, it is possible to recover the steep similarity growth given by Eq. (10), since the shape factor is held constant downstream of the switch. In a nonsimilar development, however, the variation of H_{12} is continuous. If a monotonically increasing shape factor is approximated by a series of infinitesimally small steps, the resulting growth of n will never be able to "catch up" with the value obtained from a self-similar profile at the same local shape factor and Reynolds number. The correct envelope obtained by following each frequency, therefore, will lie above the approximation of Eq. (11) without ever reaching the growth given by Eq. (10). The converse is true for an accelerating boundary layer.

Based on the preceding argument, these two envelope methods may be expected to overpredict the transition location for nonsimilar, decelerating flows and to underpredict it for nonsimilar, accelerating flows.

Stock and Degenhart's Approximate Method

Stock and Degenhart's[8] construction of the database allows the tracking of individual frequencies, thus leading to a more accurate calculation of the growth of n than afforded by the envelope methods. When used in conjunction with an integral boundary-layer method, use of the local shape factor as coupling parameter introduces an error of at most 1 n unit at any point along its growth as compared to the growth calculated with the SALLY[5] code. As discussed in Ref. 8, this error arises from the inability of H_{12} to capture the details of the velocity profile near the wall, particularly the second derivative, which has a great impact on stability calculations. If used in conjunction with a finite-difference method, on the other hand, an ingenious weighting of the shape factor with the local wall shear stress leads to a more physically meaningful coupling parameter. Since this new shape factor is a unique function of H_{12} that is easily determinable for the Falkner-Skan profiles, the same database can be utilized but with much greater accuracy. In fact, the growth of n becomes indistinguishable from that obtained with the SALLY code.

Profiles for Separated Flow

To extend the preceding theory to the prediction of transition in laminar separation bubbles, as was done in Ref. 7, it seems natural to employ the same family of profiles beyond separation as is used upstream of it, namely, the reversed Falkner-Skan, or Stewartson, profiles. As pointed out in Ref. 10, however, LDA measurements indicate that the Stewartson profiles do not reflect the actual velocity distribution in the laminar part of the bubble; rather, the measured flowfield is matched much better by the two-parameter profile family originally developed by Green[11] for a turbulent shear layer forming a free stagnation point downstream of a base. As shown in Fig. 4, the two parameters are linked to the geometrical characteristics of the profiles. The ratio (h/b) is the distance of the shear layer from the centerline of the wake, and therefore from the wall, to the width of the shear layer. G is the amplitude of Coles's wake function. Since there is slip along the centerline, these profiles cannot be utilized to develop a relationship for c_f. This shortcoming can be remedied by the skin friction correlation developed in Ref. 12 in which

a finite difference calculation of the bubble flowfield has led to very similar profiles. The skin friction coefficient obtained from this correlation is smaller than that from the Falkner-Skan profiles, as expected.

To be able to use the Green profiles, it is necessary to know how the two parameters vary inside a bubble. The measurements of Ref. 10 indicate that the amount of backflow is small (< 15% of the boundary-layer edge velocity); this is confirmed by a model that has been developed based on the work of Ref. 9. In this model the amount of pressure recovered in the laminar part of the bubble and the angle the dividing streamline makes with the airfoil surface at separation have been found to correlate well with the Gaster's pressure gradient parameter[13] and the Reynolds number based on momentum thickness at laminar separation. Knowledge of these parameters allows an accurate approximation of the pressure distribution in the laminar part of the bubble and of the location of the dividing streamline. Based on flow visualization and an analytical solution of the Navier-Stokes equations near the laminar separation point discussed in Ref. 14, the dividing streamline, in fact, is assumed to be a straight line oriented at the separation angle relative to the surface. After careful study, it was concluded that airfoil curvature has little or no effect on the so-called short or weakly interacting bubble, even near the leading edge. Remaining entirely within the approximations of conventional boundary-layer theory, therefore, there is sufficient information to correctly define the details of the flowfield in the laminar part of the bubble.

The simple geometrical definition of the Green profiles, given in Fig. 4, allows the definitions for δ_2/b and δ_3/b to be expressed explicitly in terms of the two parameters h/b and G. These relationships can be used as constraints to solve for two of the three variables h, b, and G. By forcing the net flow between the wall and the dividing streamline to equal zero, a third independent equation is obtained from which h can be determined. In this way the flowfield in the laminar part of the bubble is calculated in a manner that is consistent with conservation of mass, momentum, and energy.

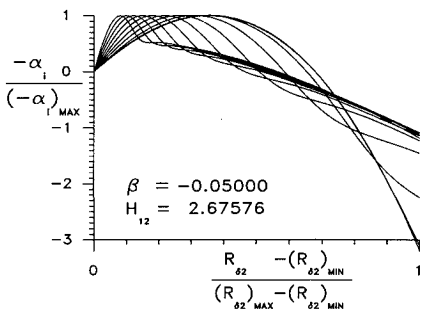

Fig. 5 Normalized amplification rate curves at constant reduced frequency.

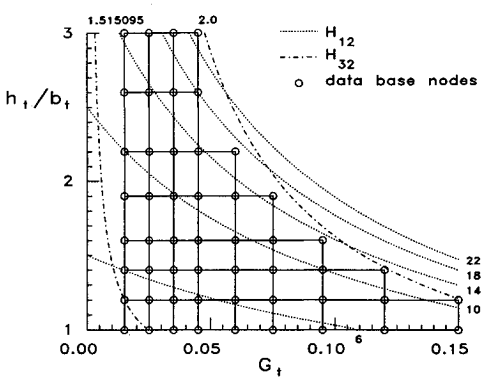

Fig. 6 Splining locus for the Green profiles.

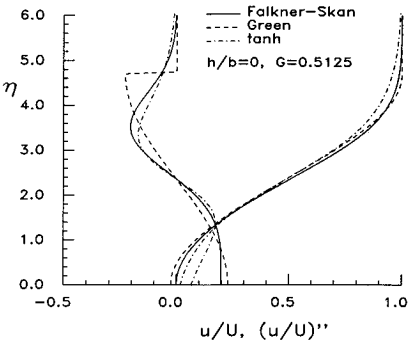

Fig. 7 Laminar separation velocity profile.

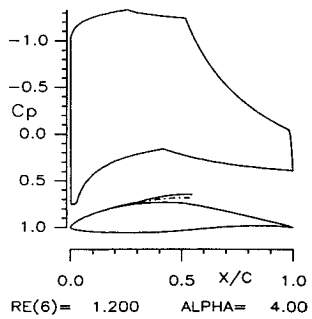

Fig. 8 Test airfoil and inviscid pressure distribution.

Without further discussion of the bubble model itself, which will appear in a separate paper, the laminar separated boundary layer has thus been approximated by a family of profiles that appears more suitable than Falkner-Skan. More importantly, the new family is general enough to allow the approximation of a wide range of flow behavior, and the present configuration can easily be improved as new measurements and insights become available (e.g., regarding the behavior of long or burst bubbles). The stability database, by contrast, already encompasses all physically plausible combinations of h/b and G values, and therefore will not have to be recomputed.

Database

As a starting point in the construction of the database, the method of Stock and Degenhart[8] has been reproduced with some slight modifications. The δ_2 is used in place of δ_1 as the characteristic thickness. Rather than storing and splining the results of Eq. (8), the dimensionless amplification rates themselves are stored and splined as functions of R_{δ_2}, H_{12}, and F. This decreases the time needed to evaluate $-\alpha_i$, which is ultimately the quantity needed in the integral for N. The determination of the amplification rate is carried beyond the crossing of the fixed reduced-frequency rays with the upper branch of the neutral curves. This is done in order to capture the relaminarization of the transitioning boundary layer that may occur, for instance, if the pressure gradient suddenly becomes very favorable downstream of the critical Reynolds number. The value of $\overline{N}$ is calculated along with α_i by means of Eq. (8), and the calculations along each ray are stopped when $\overline{N} = 0$. As is done in Ref. 8, in order to facilitate the splining of $-\alpha_i$ it is best if this function, as well as the independent variables, is normalized. This is done to ensure that the independent variables will be defined on a Cartesian grid. Figure 5 shows a set of normalized curves of $\alpha_i(R_{\delta_2}, F)$ for one value of H_{12}. In this figure, $(R_{\delta_2})_{\min}$, $(R_{\delta_2})_{\max}$, and $(-\alpha_i)_{\max}$ are functions of F. In general, they are functions of F and H_{12}. Eighteen different values of H_{12} are used between stagnation and laminar separation. Splining the stability characteristics of the Green profiles involves increasing the space

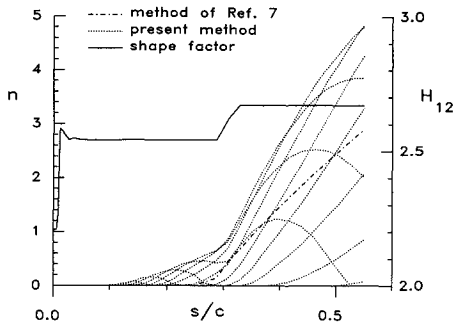

Fig. 9 Upper-surface shape factor development and comparison of upper-surface n developments for test airfoil.

of the independent variables by one dimension, corresponding to the additional parameter needed to define them.

The calculation of the stability characteristics of the Green profiles presents a problem in that these profiles have two discontinuities in curvature at the upper and lower edges of the shear layer, where the curvature abruptly goes from a maximum, given by the cosine function, to zero. This prevents the Orr-Sommerfeld equation from converging. As an approximation to the Green profiles, therefore, the hyperbolic tangent profile is utilized. This profile is more conveniently defined by means of two parameters slightly different from h/b and G, such that

$$\frac{u}{U} = \frac{1 - G_t}{2} + \frac{1 + G_t}{2} \tanh\left(y^* \frac{y - h_t}{b_t}\right) \tag{20}$$

where G_t is the amount of backflow referenced to the edge velocity, h_t is the distance from the wall to the center of the shear layer, and b_t is the half-width of the shear layer. These parameters are related to the previous ones by

$$\frac{h_t}{b_t} = 2\frac{h}{b} + 1 \tag{21}$$

$$G_t = |1 - 2G| \tag{22}$$

where the absolute-value sign is used for convenience. In Eq. (20), y^* is defined as

$$y^* = \tanh^{-1}\left[\frac{G_t - 1 + 2U_e}{G_t + 1}\right] \tag{23}$$

Unlike the Green profiles, the hyperbolic tangent profile approaches the value of 1 asymptotically. U_e in Eq. (23), therefore, is needed to specify the value of the velocity at the edge of the shear layer. Rather than prescribing an arbitrary value such as 0.99, for instance, U_e is subordinated to the coupling criteria that best match the stability characteristics of the two profiles: the amount of backflow and the slope of the shear layer at its center.

Given h/b from a knowledge of the bubble geometry, as discussed above, and H_{32} at each point in the boundary layer, the value $G(h/b, H_{32})$ is calculated from the definition of H_{32} for these profiles.[9] To ensure that these values correspond to a hyperbolic tangent profile having the same stability characteristics, the database is constructed in such a way that the slopes of two profiles with the same values of G and h/b are always equal in the center of the shear layer. This is achieved by equating the slope of a Green profile in the center of the shear layer,

$$\left(\frac{u}{U}\right)'_{y = h + b/2} = G\pi\left(\frac{h}{b} + 1\right) \tag{24}$$

to the corresponding expression derived from Eq. (20). Solving for U_e,

$$U_e = \frac{1}{2}\left[\tanh\left(\frac{\pi}{2}\right) + 1\right] + \frac{1}{2}\left[\tanh\left(\frac{\pi}{2}\right) - 1\right]G_t$$
$$= 0.958576 - 0.041424G_t \tag{25}$$

Thus, it is noted that U_e is only a function of G and is independent of h/b. Substitution of Eq. (25) into Eq. (23) yields the simple result $y^* = (\pi/2)$.

The locus of $(h_t/b_t, G_t)$ pairs used to generate the database is shown in Fig. 6. The limits on the range of h_t/b_t are set by geometrical considerations. The lower limit corresponds to the laminar separation condition, when the shear layer touches the wall, whereas the upper limit represents a distance of the shear layer from the wall not likely to be exceeded even in the thickest bubbles. The limits on the range of G_t, on the other hand, are set by the lowest and highest values that the shape factor H_{32} can achieve in a bubble: the laminar separation value, 1.515095, and 2.0, which is above most measurements. Within these limits a Cartesian grid has been laid, the intersections of which represent different amplification surfaces, $\alpha_i(R_{\delta_2}, \omega)$. If unusual and extreme conditions in a bubble were to exceed these limits, the spline evaluating routines automatically extrapolate, thereby avoiding program failure. The point corresponding to laminar separation can be recognized in the figure as the pair $(h_t/b_t = 1.0, G_t = 0.025)$. Figure 7 shows a comparison of the Falkner-Skan separation profile and its curvature distribution with its corresponding Green and hyperbolic tangent profiles. It can be seen how the hyperbolic tangent profile provides a smoother transition between the two families than do the Green profiles. From the point of view of integral boundary-layer calculations, in any case, the Green and hyperbolic tangent profiles are equivalent and shape factor and dissipation coefficient correlations could be used from either family without a noticeable difference in the results.

Each amplification rate surface is traversed by 12 constant reduced-frequency sweeps, distributed between the maximum frequency, just tangent to the neutral curve, and the minimum frequency, defined as the frequency along which $\overline{N}_{\max} = 80$, according to the rule

$$\frac{\log_{10}F - \log_{10}F_{\max}}{\log_{10}F_{\min} - \log_{10}F_{\max}} = (0, 0.05, 0.1, 0.2, \ldots, 0.9, 1) \tag{26}$$

Along each frequency, the amplification rate α_i is evaluated at 51 equally spaced points between $(R_{\delta_2})_{\min}$, at the intersection of the frequency ray with the lower branch of the neutral curve, and $(R_{\delta_2})_{\max}$, the point beyond the upper branch corresponding to the value $\overline{N} = 0$. In this way, the Reynolds number normalized between these limits has the same values for all the sweeps and all the parameter values. The presplining is performed for each frequency ray only along the direction of R_{δ_2}. The boundary-layer program uses an evaluating subroutine that fits cubic polynomials in the remaining directions to obtain the desired $\alpha_i(R_{\delta_2}, H_{12}, f)$ or $\alpha_i(R_{\delta_2}, h/b, G, f)$.

Practical Example

The test case discussed above can be examined in a more realistic setting by means of the airfoil design program presented in Ref. 15, as an arbitrary shape-factor distribution can be prescribed directly in this method. Once an airfoil that satisfies the somewhat artificial constraints given earlier has been obtained, the chord Reynolds number can be searched such that the step in shape factor occurs at the desired value of $R_{\delta_2} = 500$. Figure 8 shows an airfoil that meets these requirements at $R = 1.2 \times 10^6$ together with its inviscid pressure distribution. The boundary-layer development is driven by this inviscid distribution and the calculations are stopped at the

end of the rooftop, or the second constant-H_{12} segment. Along the surface of the airfoil the actual n developments themselves are shown, plotted in units of percent chord above corresponding y coordinates. The solid line represents the envelope of 20 frequencies calculated by the present method, while the dotted-dashed line is calculated by means of the method of Ref. 7. Figure 9 shows the shape factor distribution actually achieved together with the predicted n developments, this time comparing the prediction of Ref. 7 to all 20 frequencies. It should be pointed out that part of the difference between the two methods is due to a mismatch in critical Reynolds number. In Ref. 7, the critical Reynolds number is calculated according to a curve-fit whose accuracy decreases in favorable gradients. Even if this minor and conceptually unimportant problem were eliminated, such that along the first constant-H_{12} segment the two methods coincided, downstream of the switch there would still be a noticeable difference.

Comparisons with Measurements

The accuracy of the present method for attached boundary layers is discussed at length in Ref. 8. In this paper, therefore, comparisons are made with measurements of transition locations inside laminar separation bubbles, as well as with the corresponding predictions obtained with the envelope method of Ref. 7. To make these comparisons more meaningful, it is necessary to discuss briefly how the boundary-layer development is calculated.

Although the present method can be used in a variety of viscous analysis methods for incompressible airfoil flows, it was developed with the purpose of incorporating it into the airfoil design and analysis program of Eppler and Somers.[16] In fact, the laminar separation bubble model discussed in Ref. 9 has been included in this program and is currently used in conjunction with the present transition prediction method

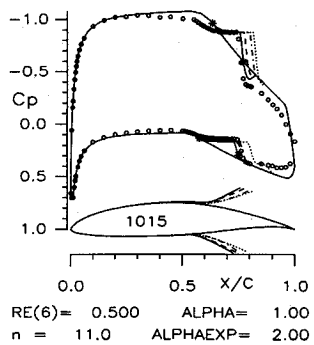

Fig. 10 Comparison of transition prediction inside the bubble. Solid line, present method (Green profiles); dashed line, present method (Falkner-Skan profiles); dotted-dashed line, envelope method[7]; dotted line, corrected envelope method. Data are from Ref. 18.

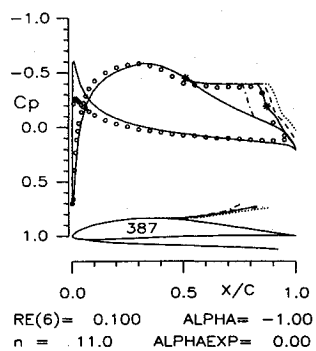

Fig. 11 Comparison of transition prediction inside the bubble. Solid line, present method (Green profiles); dashed line, present method (Falkner-Skan profiles); dotted-dashed line, envelope method[7]; dotted line, corrected envelope method. Data are from Ref. 19.

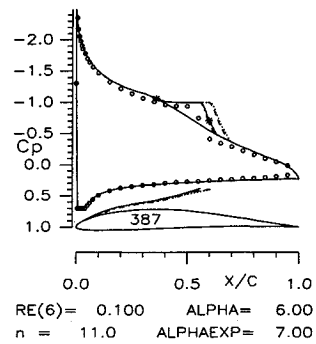

Fig. 12 Comparison of transition prediction inside the bubble. Solid line, present method (Green profiles); dashed line, present method (Falkner-Skan profiles); dotted-dashed line, envelope method[7]; dotted line, corrected envelope method. Data are from Ref. 19.

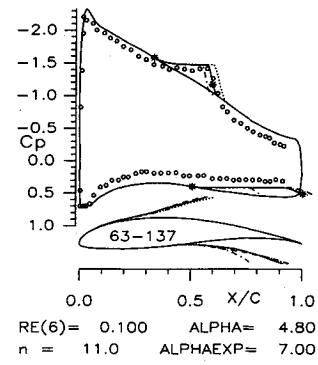

Fig. 13 Comparison of transition prediction inside the bubble. Solid line, present method (Green profiles); dashed line, present method (Falkner-Skan profiles); dotted-dashed line, envelope method[7]; dotted line, corrected envelope method. Data are from Ref. 21.

for routine analyses during the airfoil design process. The program of Eppler and Somers employs a conformal mapping method that allows multipoint design by specifying different characteristics of the velocity distribution over different segments of the airfoil. The exact inviscid distribution thus obtainable is then analyzed by means of an integral boundary-layer method utilizing the momentum and energy integral equations. Although a single displacement thickness iteration can be prescribed for calculating the zero-lift angle of attack more accurately, this option is seldom used. In fact, assuming that the boundary layer and outer flows are interacting weakly yields very accurate drag polars for an extremely small computational cost. The fact that at a particular angle of attack the inviscid and experimental pressure distributions do not match is of no consequence since airfoils are designed by specifying desired characteristics at particular lift coefficients and are compared by means of drag polars. Near maximum lift, of course, the viscous/inviscid interaction is not weak, but this program utilizes an approximation for the effects of turbulent separation that, given enough experience on the part of the designer, has led to a number of very successful airfoils that have been operating on gliders, general aviation aircraft, business-class turboprops, wind turbines, marine propellers, and model airplanes for over three decades.[17]

The laminar separation bubble model of Ref. 9 and the transition prediction method discussed in this paper were developed to improve the drag prediction accuracy of the Eppler and Somers program for chord Reynolds numbers smaller than 2×10^6. The laminar separation bubble model is based on the assumption that the strong interaction is limited to the immediate vicinity of the bubble. This allows the utilization of the inviscid velocity distribution everywhere else, thus keeping computational requirements within bounds to be useful for airfoil design. As discussed in detail in Ref. 9, the bubble

model relies on an approximation to the pressure distribution in the laminar part of the bubble that has been successfully correlated to many measured pressure distributions on different airfoils at different Reynolds numbers. This allows the calculation of the boundary-layer development in the laminar part of the bubble in the direct mode and without making recourse to an interaction algorithm. The turbulent part is calculated by prescribing a distribution of H_{32} and solving the momentum and energy integral equations in the inverse mode. The transition location can be recognized by the sharp corner in the bubble pressure distribution. Although transition initiates upstream of this corner and occurs over a small but finite region of the airfoil, in the present method it is assumed to occur at a point.

In order to compare the methods discussed earlier exhaustively, it is necessary to present four separate predictions for all the cases shown in the following figures. A different line type is shown in the plots to depict the amplification factor growth along the airfoil surface as calculated by each different method. The same line type is also used to indicate the corresponding bubble pressure distribution. For all these cases the inviscid pressure distribution is used to drive the boundary layer upstream and downstream of the bubble. A solid line is used for the present method utilizing the Green profiles. For the sake of completeness, the present method has also been applied to the reversed Falkner-Skan profiles, and the corresponding curves are shown by a dashed line. This allows the comparison between the method of Ref. 7 and the present method also inside the bubble and with the same family of profiles. The solid and dashed curves represent the numerically calculated envelopes of twenty frequencies calculated individually in each case. The envelope method of Ref. 7 is shown in a dotted-dashed line. This method has been found to contain some additional errors due to inaccurate curve fitting of Eq. (10) for very high values of H_{12}. A corrected version has been kindly provided and is shown here as a dotted line.

Figure 10 shows a comparison with data taken from the NASA NLF(1)-1015 airfoil at $R = 500{,}000$ (Ref. 18). The bubble model used in conjunction with the present transition prediction method is invoked when laminar separation is encountered by the boundary layer as driven by the inviscid velocity distribution. The asterisks denote the laminar separation and the turbulent reattachment points. It can be seen how the presence of the bubble modifies to some extent the upper-surface inviscid pressure distribution upstream of laminar separation. Therefore, some error in the predicted transition location should be ascribed to the different impact these two distributions have on the growth of n. This airfoil poses an additional challenge in that it is markedly aft loaded, leading to greater discrepancies between the inviscid and the measured pressure distributions as the trailing edge is approached. Whereas the upper-surface bubble as calculated with the present method is of the right length, the transition location in the lower surface bubble is underpredicted. Rather than a shortcoming of the transition method, the disagreement is due to the difference between the experimental pressure gradient, softened by the strong trailing-edge interaction, and the inviscid one, which drives the bubble model.

The dotted-dashed line in Fig. 10 corresponds to the envelope method of Ref. 7. Before laminar separation, the two methods are almost identical. Since this has been observed for all the airfoils analyzed, it can be said that the shape factor distributions characteristic of most airfoil flows are smooth enough to warrant the approximation implied by Eq. (11) and, therefore, that the envelope method of Ref. 7 is sufficiently accurate before laminar separation. However, as shown by the difference between the present method applied to the reversed Falkner-Skan profiles (dashed line) and the envelope method, the steep growth of shape factor inside the bubble leads to a significant error in the calculation of n by the latter. A more significant example of this effect is given by the new, corrected envelope method shown as the dotted line. These comparisons confirm the error trend due to the nonsimilar development discussed earlier for the test case.

As a second example, Fig. 11 shows a comparison with the experimental pressure distribution of the Eppler E387 airfoil at a chord Reynolds number of 100,000 and $\alpha = -1$ deg (Ref. 19). This angle was chosen in order to match the measured upper-surface pressure distribution as closely as possible. The same trends are observed again here, with the curve-fitting errors of the original envelope method (dotted-dashed line) becoming drastically apparent. Indeed, this example shows why such large values of n_{crit} are necessary to match measured bubble lengths when the original envelope method is used at very low Reynolds numbers.[20] All four curves coincide for the lower surface boundary-layer development, which is all attached. Thus far, it appears that the Falkner-Skan profiles, if used properly, can achieve a reasonably accurate approximation of the flowfield. However, Fig. 12 shows that this is not the case. For the same airfoil at the same Reynolds number but at $\alpha = 6$ deg, the present method with the Green profiles is more accurate than the others. Fortuitously, the original envelope method is more accurate in this case because of the same curve-fitting problem discussed above. Last, Fig. 13 shows a comparison with the pressure distribution of the Wortmann FX63-137 airfoil at $R = 100{,}000$ and $\alpha = 4.8$ deg (Ref. 21). Although for the previous airfoils the exact inviscid velocity distribution is generated simultaneously with the coordinates by the conformal mapping method used by the Eppler and Somers program, in this case it is obtained by means of a higher-order panel method also employed by the program.[16] The upper-surface bubble is predicted well by the present method as well as by the Falkner-Skan profiles, whereas the original envelope method leads to an underprediction. The same effect, but more drastic, is observed in the lower-surface bubble, which extends to the trailing edge.

From the preceding comparisons, it appears that the highly nonsimilar flow inside the bubble leads to unacceptable errors when the envelope method, even the corrected one, is used. The Falkner-Skan profiles used in conjunction with the present method, on the other hand, give reasonably accurate results in five out of the six bubbles examined. The present method with the Green profiles, however, gives the best and most consistent transition prediction accuracy. These results also serve to show how the very large values of n_{crit}, on the order of 20, reported in Ref. 20 are not due to low-Reynolds-number or freestream turbulence effects but, rather, to a curve-fitting error present in the original envelope method. In all of these comparisons $n_{crit} = 11$ was used. The present method with the Green profiles has been used with the same value of n_{crit} also at Reynolds numbers higher than those shown here, with the same degree of accuracy in the results.

Conclusions

Although the present method of transition prediction has been shown to be more accurate than envelope methods for nonsimilar boundary-layer developments, shape factor distributions typically found on airfoils are smooth enough for envelope methods to remain sufficiently accurate for attached boundary layers. The present transition prediction method is still necessary for separated flows, however, as the shape factor growth is too steep for any assumption of local similarity to hold. In addition, envelope methods cannot be applied to an arbitrarily defined family of profiles such as the Green profiles, which approximate the flowfield in the laminar part of the bubble more accurately than the Falkner-Skan family. The new database developed for attached and separated boundary layers is very general and can be used in conjunction with any two-dimensional airfoil viscous analysis method. Specification of the correct flowfield geometry in the laminar part of the bubble has led to accurate predictions of bubble lengths with the same value of critical amplification factor for all Reynolds numbers at which bubbles occur.

Acknowledgments

Use of the hyperbolic tangent profile and of its coupling criteria to the Green profiles was suggested by P. J. Morris of the Pennsylvania State University. The corrected version of the envelope method was kindly provided by M. Drela of the Massachussetts Institute of Technology.

References

[1]Michel, R., "Etude de la Transition et Calcul de la Trainée des Profils d'aile en Incompressible," ONERA Publ. 58, 1951.

[2]Eppler, R., "Practical Calculation of Laminar and Turbulent Bled-Off Boundary Layers," NASA TM-75328, 1978 (translated from *Ingenieur Archiv,* Vol. 32, 1963, pp. 221–245).

[3]Van Ingen, J. L., "A Suggested Semi-Empirical Method for the Calculation of the Boundary Layer Transition Region," Delft Univ. of Technology, Dept. of Aerospace Engineering Rept. VTH-74, Delft, The Netherlands, 1956.

[4]Smith, A. M. O., and Gamberoni, N., "Transition, Pressure Gradient, and Stability Theory," Douglas Aircraft, Rept. ES 26338, Long Beach, CA, 1956.

[5]Skrokowski, A. J., Orzag, S. A., Kaups, K., and Cebeci, T., "A FORTRAN Program to Compute and Integrate Disturbance Amplification Rates on Swept and Tapered Laminar Flow Control Wings with Suction," COSMIC, Univ. of Georgia, Athens, GA, 1979.

[6]Gleyzes, C., Cousteix, J., and Bonnet, J. L., "A Calculation Method of Leading Edge Separation Bubbles," *Numerical and Physical Aspects of Aerodynamic Flows II,* edited by T. Cebeci, Springer-Verlag, New York, 1983, pp. 173–192.

[7]Drela, M., and Giles, M. B., "Viscous-Inviscid Analysis of Transonic and Low-Reynolds Number Airfoils," *AIAA Journal,* Vol. 25, No. 10, 1987, pp. 1347–1355.

[8]Stock, H. W., and Degenhart, E., "A Simplified e^n Method for Transition Prediction in Two-Dimensional, Incompressible Boundary Layers," *Zeitschrift Flugwiss, Weltraumforsch,* Vol. 13, 1989, pp. 16–30.

[9]Dini, P., "A Computationally Efficient Modelling of Laminar Separation Bubbles," Ph.D. Dissertation, Dept. of Aerospace Engineering, Pennsylvania State Univ., University Park, PA, 1990.

[10]Fitzgerald, E. J., and Mueller, T. J., "Measurements in a Separation Bubble on an Airfoil Using Laser Velocimetry," *AIAA Journal,* Vol. 28, No. 4, 1990, pp. 584–592.

[11]Green, J. E., "Two-Dimensional Turbulent Reattachment as a Boundary-Layer Problem," *Separated Flows,* AGARD CP 4, Pt. 1, May 1966, pp. 393–426.

[12]Drela, M., "Improvements in Low Reynolds Number Airfoil Flow Predictions with ISES and XFOIL," Massachusetts Inst. of Technology, CFL Rept. 91-5, Cambridge, MA, 1991.

[13]Gaster, M., "The Structure and Behavior of Separation Bubbles," Aeronautical Research Council R. & M. No. 3595, United Kingdom, March 1967.

[14]Van Ingen, J. L., and Boermans, L. M. M., "Aerodynamics at Low Reynolds Numbers: A Review of Theoretical and Experimental Research at Delft University of Technology," *International Conference on Aerodynamics at Low Reynolds Numbers* $10^4 < R < 10^6$, Vol. I, Royal Aeronautical Society, London, Oct. 1986, pp. 1.1–1.40.

[15]Selig, M. S., and Maughmer, M. D., "Generalized Multi-Point Inverse Airfoil Design," AIAA 9th Applied Aerodynamics Conf., AIAA Paper 91-3333, Baltimore, MD, Sept. 1991.

[16]Eppler, R., and Somers, D. M., "A Computer Program for the Design and Analysis of Low-Speed Airfoils," NASA TM-80210, 1980.

[17]Eppler, R., *Airfoil Design and Data,* Springer-Verlag, New York, 1990.

[18]Maughmer, M. D., and Somers, D. M., "Design and Experimental Results for a High-Altitude, Long-Endurance Airfoil," *Journal of Aircraft,* Vol. 26, No. 2, 1989, pp. 148–153.

[19]McGhee, R. J., Walker, B. S., and Millard, B. F., "Experimental Results for the Eppler 387 Airfoil at Low Reynolds Numbers in the Langley Low-Turbulence Pressure Tunnel," NASA TM-4062, Oct. 1988.

[20]Evangelista, R., and Vemuru, C. S., "Evaluation of an Analysis Method for Low-Speed Airfoils by Comparison with Wind Tunnel Results," AIAA Paper 89-0266, Jan. 1989.

[21]Brendel, M., and Mueller, T. J., "Boundary Layer Measurements on an Airfoil at Low Reynolds Numbers," *Journal of Aircraft,* Vol. 25, No. 7, 1988, pp. 612–617.